

Improving wear resistance of 3D printed alumina-based ceramics via sintering temperature

Jing-wen Sun^{1,2}, *He Li^{1,2}, Yun-song Mu^{1,2}, **Bao-xia Mu³, Yan-hua Chen^{1,2}, and Paolo Colombo⁴

1. School of Materials Science and Engineering, Xinjiang Key Laboratory of Solid State Physics and Devices, Xinjiang University, Urumqi 830046, China

2. School of Materials Science and Engineering, Xinjiang Environmental and Functional Materials Engineering Research Center, Xinjiang University, Urumqi 830046, China

3. School of Physics Science and Technology, Xinjiang University, Urumqi 830046, China

4. Department of Industrial Engineering, University of Padova, Padova 35131, Italy

Copyright © 2025 Foundry Journal Agency

Abstract: Ceramic materials with intricate structures can be efficiently fabricated using stereolithography (SLA) based 3D printing technology, offering advantages over traditional methods. Sintering temperature has primary effect on properties of ceramics. This study investigated the crucial sintering temperature for 3D printed ceramics to ensure the desired properties. The results indicate that all samples exhibit a consistent layered structure across the experimental sintering temperatures. When the sintering temperature is increased from 1,250 °C to 1,350 °C, the grain's morphology changes from spherical to plate-like. Surface morphology analysis reveals a decrease in surface roughness at sintering temperatures above 1,350 °C. Mechanical tests show improved flexural strength and stiffness as the sintering temperature rises. Friction and wear experiments demonstrate that as the sintering temperature increases from 1,450 °C to 1,550 °C, the wear pattern on ceramic surfaces transitions from deep pits to shallow grooves. The increase in sintering temperature effectively enhances the wear resistance of 3D printed alumina ceramics. This improvement plays a significant role in expanding the application field of these ceramics, prolonging the lifespan of parts, reducing production costs, enhancing performance, and promoting environmental protection. In this study, ceramics achieve the highest strength and best wear resistance when sintered at 1,600 °C, resulting in the best overall performance.

Keywords: sintering temperature; friction and wear properties; stereolithography; alumina ceramics

CLC numbers: TG146.21

Document code: A

Article ID: 1672-6421(2025)02-151-12

1 Introduction

Alumina is a versatile ceramic material that is renowned for its exceptional insulating qualities, high hardness, strength, stiffness, chemical stability, and outstanding optical transparency. Alumina ceramics are widely utilized across diverse industries for applications in electronics, abrasive tools, chemical reactors, refractory and high-temperature heating apparatus, optical components, among others^[1, 2]. Alumina exhibits high hardness, making it well-suited for friction materials

due to its high wear and scratch resistance^[3, 4]. Proper formulation of materials and sintering processes can enhance the density and mechanical properties of alumina ceramics, thereby improving their friction and wear performance. More and more scholars have investigated the friction and wear characteristics of ceramics. Doi et al.^[5] concluded that the shape and size of the particles control the formation of the interfacial friction film. The hardness, composition, size, shape, and type of ceramic particles are the primary factors that affect friction and wear performance. Matějka et al.^[6] systematically investigated the influence of silicon carbide content on the friction and wear properties. The results indicate that the coefficient of friction (COF) and wear resistance of the material increased with an increase in particle content. The current research focuses on the impact of particle characteristics on friction and wear performance. However, there are few studies on the impact of sintering temperature on the

*He Li

Ph. D., Associate Professor. Her research interests mainly focus on the ceramic additive manufacturing technology.

E-mail: lihe@xju.edu.cn

**Bao-xia Mu

E-mail: mbxmbb@xju.edu.cn

Received: 2023-11-13; Revised: 2024-04-07; Accepted: 2024-07-10

friction and wear performance of ceramics.

Traditionally, alumina ceramics are manufactured through processes such as pressing, injection molding, and sintering. The emergence of 3D printing technology has revolutionized alumina ceramics production, offering unparalleled design flexibility and freedom. This method provides precise control over layer-by-layer fabrication, allowing the creation of complex geometries with improved efficiency [7,8]. As shown in Fig. 1, stereolithography (SLA) is a technology used for the additive manufacturing of three-dimensional objects by sequentially curing a photosensitive liquid polymer using ultraviolet light, layer by layer [9,10]. After 3D printing, the completed ceramics typically requires high temperature sintering to achieve the intended strength and density. The appropriate sintering temperature promotes inter-particle bonding, enabling the print to achieve a dense structure at high temperatures and preventing the occurrence of internal cracks and deformation [11]. Different manufacturing methods and specific requirements may result in variations in sintering temperatures for practical applications.

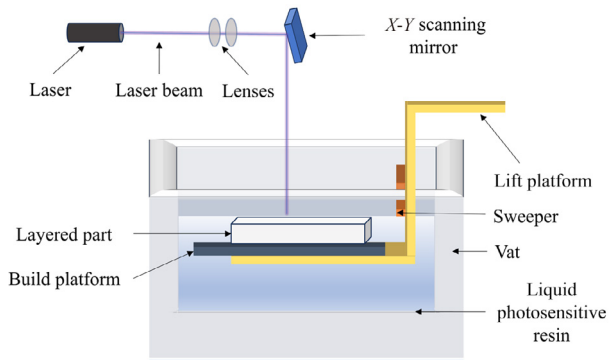


Fig. 1: Schematic diagram of stereolithography 3D printing equipment

Researchers have explored factors influencing the performance of alumina ceramics manufactured through SLA technology. Li et al. [12] investigated the effect of debinding holding time on the mechanical properties of alumina ceramic cores. They found that the ceramic cores exhibited the best mechanical properties when debinding under vacuum for 120 min and under argon for 180 min. Zhou et al. [13] utilized PEG400 as a liquid desiccant and compared various drying and debinding processes to minimize distortion of green bodies. A two-step debinding process using vacuum pyrolysis and air debinding can effectively control the pyrolysis rate and prevent the formation of defects in the Al_2O_3 body. Sintering temperature is a crucial factor in ensuring the structural stability of 3D printed ceramics during the sintering process. Sintering in the appropriate temperature range can eliminate pores and defects, improve the density of ceramic parts, and enhance their mechanical properties [14]. Li et al. [15] studied the effect of sintering temperature on the mechanical properties of 3D printed alumina ceramics and found that as the sintering temperature increased, spherical grains transformed into cylindrical grains. In addition, due to the high sintering temperature, ceramic parts became highly dense after sintering

at temperatures exceeding 1,500 °C, resulting in a significant improvement in the strength of ceramics. Yang et al. [16] utilized an orthogonal test method to examine the impact of sintering temperature on the characteristics of alumina ceramics. They discovered that the highest flexural strength (458.1 MPa) was achieved at a sintering temperature of 1,550 °C. This was due to a combination of small grain size, close contact between grains, and high relative density. At present, most research focuses on the relationship between sintering temperature and sample flexural strength, while few studies concentrate on friction and wear properties [17,18]. The wear resistance of ceramics is crucial for ensuring their stability and durability in harsh environments, such as high temperatures and high pressures. This is especially important for applications where wear and fatigue resistance are vital, such as turbine blades, ceramic bearings, cutting tools, brake pads, artificial joints, and so on. The exceptional wear resistance of ceramics enhances the performance, durability, and reliability of equipment and products. Furthermore, maintenance and replacement expenses are reduced, leading to a positive impact on the sustainability of industries such as transportation, and healthcare. Therefore, in this study, a comprehensive investigation was conducted to explore the relationship between the sintering temperature and various properties of alumina ceramics produced using the stereolithography based 3D printing technology, including their microstructure, physical characteristics, mechanical properties, friction and wear behaviors.

2 Experimental

2.1 Experimental materials

Al_2O_3 powder ($\alpha\text{-Al}_2\text{O}_3$) was mixed with a photosensitive resin to create an alumina ceramic slurry with a solid content of 50vol.%. The photoresin mixture consisted of 70wt.% of a monofunctional monomer (5-ethyl-1,3-dioxan-5-yl) (CTFA) and 30wt.% of a trifunctional monomer of trimethylolpropane triacrylate (TMPTA). Alumina green bodies (50 mm×5 mm×4 mm) were printed using a 3D printer with a layer thickness of 75 μm and a single-layer exposure time of 2 s. Figure 2 shows the design model of the sample body and the printed sample.

2.2 Debinding and sintering

Figure 3 shows the curve of the debinding and sintering procedures of green bodies. The green bodies were debinded in air using a muffle furnace (HG-17-4B, Shanghai Hegong Scientific Instrument Co., Ltd., China). The process began with heating the green bodies to 200 °C at a rate of 2 °C·min⁻¹. Subsequently, the samples were heated to 600 °C at a rate of 1 °C·min⁻¹ and held at this temperature for 2 h. Afterward, the samples underwent further heating to various temperatures: 1,150 °C; 1,250 °C; 1,350 °C; 1,450 °C; 1,550 °C; and 1,650 °C, each at a rate of 5 °C·min⁻¹, with a dwell time of 2 h at each temperature. Finally, the temperature was reduced to 600 °C at a rate of 5 °C·min⁻¹, and the samples were cooled to room temperature as the furnace cools down.

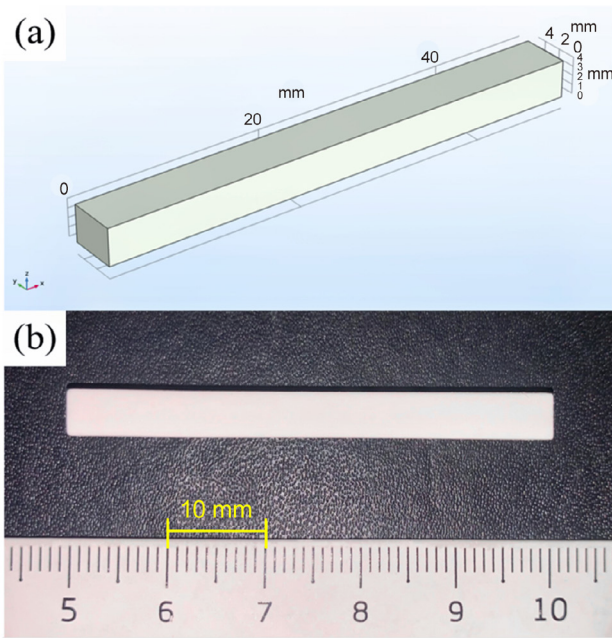


Fig. 2: Design model (a) and printed green sample (b)

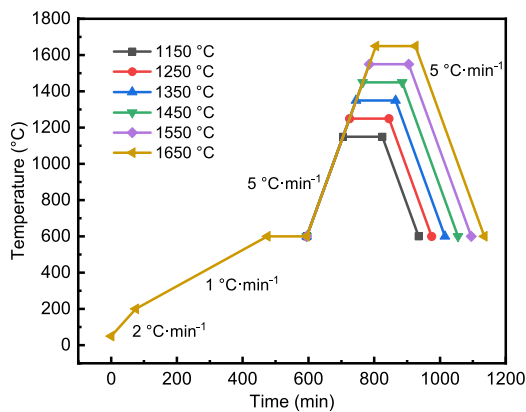


Fig. 3: Debinding and sintering procedures of green bodies

2.3 Characterization methods

To assess the impact of sintering temperature on stereolithography-based 3D printed alumina ceramics, an analysis was conducted on the microstructural, physical, mechanical, friction, and wear properties of the samples. The thermal analysis (DSC404F1, Netzsch, Germany) of the green body was conducted under high purity argon gas with a heating rate of $10\text{ }^{\circ}\text{C}\cdot\text{min}^{-1}$ from $30\text{ }^{\circ}\text{C}$ to $1,000\text{ }^{\circ}\text{C}$. The microstructures of the workpieces were determined using a scanning electron microscopy (GeminiSEM 300, ZEISS, Germany). The microcomputer-controlled electronic universal testing machine (ETM105D, Shenzhen Wanji Testing Equipment Co., Ltd.) was used to determine the flexural strength of specimens at various temperatures. The machine utilized a loading speed of $0.5\text{ mm}\cdot\text{min}^{-1}$ and a span length of 37.89 mm . The samples were tested and analyzed using a multifunctional friction and wear tester (MFT-2000, RTEC, USA). The experimental friction force was 5 N , the friction frequency was 5 Hz , and the test duration was 10 min . The 6.35 mm diameter zirconia balls were used for the tests. The surface morphology of the samples after sintering and after friction wearing was examined using

a three-dimensional optical profilometer (UP-2000, RTEC, USA). Open porosity and bulk density of the specimen were determined using the Archimedes' method. The Eqs. (1) and (2) can be used to calculate the bulk density and open porosity of the samples, respectively ^[19]:

$$B = \frac{G_2 - G_1}{G_2 - G_3} \times 100\% \quad (1)$$

$$d = \frac{G_1 \times d_w}{G_2 - G_3} \quad (2)$$

where B represents the open porosity percentage (%) of the specimen, d is the specimen's bulk density ($\text{g}\cdot\text{cm}^{-3}$), d_w is the density of water at the test temperature ($\text{g}\cdot\text{cm}^{-3}$), G_1 is the dry specimen's mass (g), G_2 is the specimen's mass in air after saturated with water (g), and G_3 is the specimen's mass in water after saturated with water (g).

3 Results and discussion

3.1 DSC analysis

Figure 4 shows the DSC results of the green bodies. The DSC curve illustrates the heat changes resulting from the chemical reaction during the decomposition of photosensitive resin as the temperature rises. The decomposition temperature range can be divided into three stages: $30\text{ }^{\circ}\text{C}$ – $200\text{ }^{\circ}\text{C}$, $200\text{ }^{\circ}\text{C}$ – $600\text{ }^{\circ}\text{C}$, and $600\text{ }^{\circ}\text{C}$ – $1,000\text{ }^{\circ}\text{C}$, based on the DSC curves. Among them, exothermic peaks appear at around $65\text{ }^{\circ}\text{C}$ and $140\text{ }^{\circ}\text{C}$ in the first stage, indicating that the samples undergo exothermic reactions in these temperature ranges. During the initial stages of the sintering process, the volatile organic solvents in the photosensitive resin remaining in the ceramic body may volatilize within this temperature range, leading to exothermy. In addition, the monomers in photosensitive resins undergo polymerization reactions in this temperature range, forming a polymer network structure. This process may also release heat and lead to the emergence of exothermic peaks. There is a second-stage exothermic peak at around $450\text{ }^{\circ}\text{C}$, and the photosensitive resin undergoes exothermic reactions when heated in argon gas. The decomposition of TMPTA at high temperatures with sufficient oxygen, as shown in reaction Eq. (3), produces carbon oxides, including carbon monoxide (CO) and carbon dioxide (CO_2), as well as some volatile organic compounds with low molecular weight, such as acrylic acid, acrolein, etc. Additionally, it generates carbon black or other carbide particles. At very high temperatures, CTFA will also undergo severe thermal decomposition, as shown in the reaction of Eq. (4), which produces carbon oxides such as carbon monoxide (CO) and carbon dioxide (CO_2), low-carbon olefins such as ethylene and propylene, volatile organic compounds with low molecular weight such as acrylic acid and formaldehyde, and various decomposition products of carbon black or other carbon compounds ^[20]. The organic binder in the green bodies primarily decompose between 350 and $500\text{ }^{\circ}\text{C}$. It has been demonstrated that photosensitive resins experience

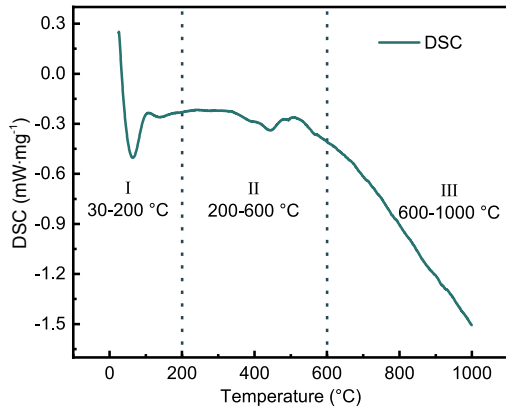
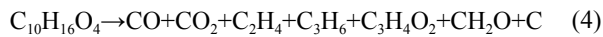


Fig. 4: DSC curves of alumina green bodies

thermal decomposition at temperatures below 450 °C, and their thermal decomposition process is essentially completed at 600 °C^[21], consistent with the findings obtained in this study.



Meanwhile, there is a fluctuation in the curve between 500–600 °C, which could be attributed to the release of a large amount of gas by the photosensitive resin after an exothermic reaction. This gas could not be immediately released, leading to an increase in the gas density inside the crucible. This phenomenon increases the buoyancy force acting on the sample. When the gas is eventually released, the density of the gas inside the furnace decreases, thereby reducing the buoyancy force acting on the sample.

Sotov et al.^[22] utilized TGA-DSC analysis to determine thermal debinding parameters to obtain crack-free samples, and they found that most of the resin decomposed rapidly between 300 °C and 525 °C. Dong et al.^[23] fabricated BCP bioceramics with excellent densification and mechanical properties using

SLA 3D printing, with most of the decomposition of the ceramic green bodies occurring between 200 °C and 500 °C, and the resin almost completely decomposing at 550 °C. Yu et al.^[24] introduced $\text{Ca}(\text{OH})_2\text{-MgO-SiO}_2$ as a sintering additive to enhance the properties of alumina ceramics, and they found that the organics began to decompose and release heat at 200 °C. Above 500 °C, the sample's mass remained essentially unchanged, indicating complete decomposition of organic matter and completion of the debinding process. Under the same conditions where stereolithography was used to print ceramics, it was observed that the decomposition reaction of photosensitive resin took place between 200–600 °C, with a concentration in the range of 350–500 °C. These findings are consistent with the temperature ranges of 300–525 °C, 200–550 °C, and 200–500 °C reported in the three works mentioned above. Debinding has a significant impact on the quality of formed 3D printed ceramics. According to reaction Eqs. (3) and (4), these residues will decompose at high temperatures to produce CO, CO₂, and other gases. This leads to an increase in the internal pressure of the ceramics. Simultaneously, thermal stress, gravity, and residual stress acting on the green body contribute to the formation of cracks. Poor control of process parameters can also lead to crack formation. When the debinding rate is too fast, the alumina green body is subjected to sharp changes in temperature and stress concentrations in localized areas, which can result in cracks. Therefore, to prevent the rapid reaction rate of organic matter and subsequent gas production that can lead to imperfections such as holes and cracks in green bodies, as illustrated in Fig. 3, it is advisable to reduce the heating rate during the debinding process as much as possible.

3.2 Microstructure and surface topography

Figure 5 displays the SEM images of the ceramic samples sintered at 1,250 °C; 1,350 °C; 1,550 °C; and 1,650 °C, respectively. Conducting research on the mechanisms of crystal

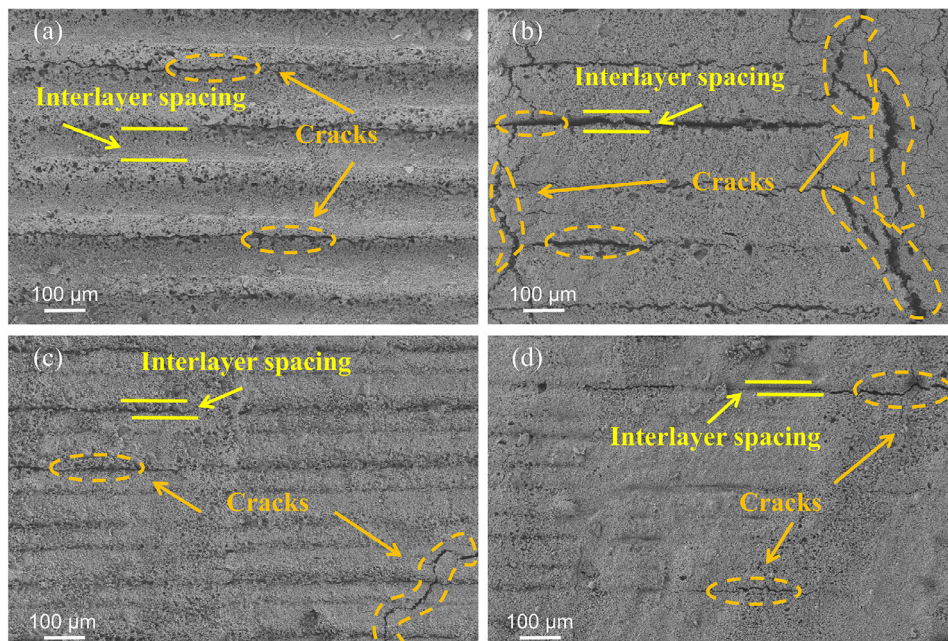


Fig. 5: Lateral SEM images of ceramic samples after sintering at 1,250 °C (a); 1,350 °C (b); 1,550 °C (c); 1,650 °C (d)

formation and growth, as well as investigating the density and porosity characteristics of materials, holds paramount importance. Figure 5 reveals that at a lower sintering temperature of 1,250 °C, the ceramic surface exhibits a considerable quantity of pores, characterized by larger pore diameters. With an elevation in sintering temperature to 1,650 °C, a notable reduction in the observable pores on the ceramic surface is observed. Furthermore, the pore diameters decrease, resulting in a smoother surface for the samples. The samples exhibit layer delamination after sintering at all four temperatures. In some similar studies on SLA-3D printed ceramics, the sintered ceramics also exhibit delamination [25-27]. This issue can be attributed to the layer-by-layer printing process used in 3D printing [28], which results in inadequate adhesion between ceramic layers and subsequent delamination after sintering. After undergoing sintering at each temperature, the samples exhibit varying degrees of cracking. The most severe cracking is observed at 1,350 °C, where cracks in the Z-direction

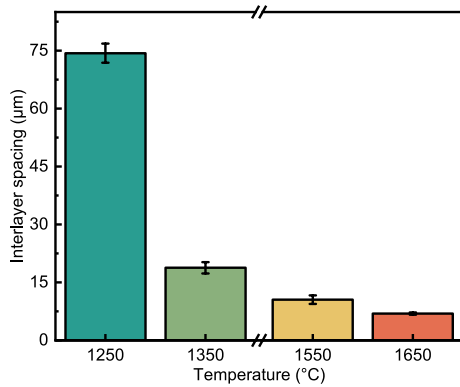


Fig. 6: Interlayer spacing of ceramic samples sintered at different temperatures

penetrate the X-Y plane. This phenomenon maybe caused by the thermal expansion and contraction that occur in ceramic materials during the sintering process. The delamination of 3D printed ceramics may lead to uneven heat conduction between ceramic particles, resulting in an irregular temperature distribution in the ceramic body during sintering. The uneven distribution of temperature results in the accumulation of stress within the material, leading to the formation of cracks in the ceramic samples. Figure 6 displays the interlayer spacing of the samples at each sintering temperature measured in Fig. 5. It is noticeable that the interlayer spacing decreases as the sintering temperature increases. This indicates that elevated temperatures during sintering are more conducive to the rearrangement of ceramic particles, resulting in a denser material. The increased temperature facilitates material migration to fill the pores, thereby further decreasing the interlayer spacing. In addition, ceramic materials experience sintering shrinkage as the temperature increases during the sintering process [29], leading to a gradual reduction in the spacing of the printed layers.

Figure 7 shows the SEM images of the cross-section of the ceramic samples after sintering at 1,250 °C; 1,350 °C; 1,550 °C; and 1,650 °C, respectively. When sintered at 1,250 °C, the samples contained randomly arranged spherical grains of varying sizes. After sintering at a lower temperature, the contact between the spherical ceramic particles are minimal, resulting in loose connections and the presence of numerous pores within the ceramic matrix. Consequently, this yields high open porosity and insufficient density in the ceramic body. When sintered at 1,350 °C, the grain morphology transforms from spherical to plate-like, accompanied by an expansion of pore size within the sample. The emergence of larger pores

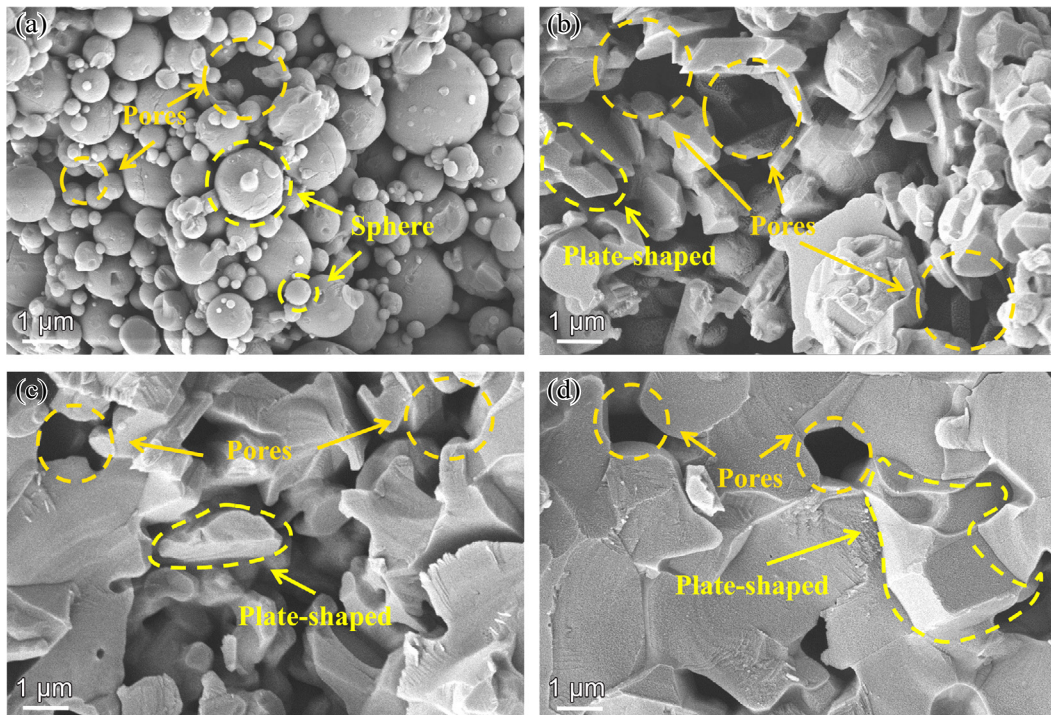


Fig. 7: Cross-sectional SEM images of ceramic samples after sintering at 1,250 °C (a); 1,350 °C (b); 1,550 °C (c); 1,650 °C (d)

and cracks contribute to the increase in porosity and decrease in bulk density following sintering at 1,350 °C. As the sintering temperature rises, the solid particles bond together, the grains grow, the voids and grain boundaries gradually reduce, and the overall volume shrinks, leading to an increase in density due to mass transfer phenomena^[30]. As indicated by the SEM images, at a sintering temperature of 1,650 °C, the particles within the sample are strongly fused together, and the pores become more rounded and their quantity decreases. At elevated temperatures, there is a greater driving force for ceramic sintering. An increase in sintering temperature boosts the activity and diffusion rate of ceramic particles, enabling them to possess higher thermal energy. Consequently, they can diffuse and rearrange more rapidly at high temperatures. This results in a significant reduction in ceramic porosity, effectively enhancing bulk density.

Figure 8 shows the trend in the average particle size of the samples at different sintering temperatures. It illustrates a gradual increase in particle size as temperature rises. The driving force in the sintering process is the reduction of the free energy of the system. The sintering neck is the region between two adjacent particles that come into contact with one another and grow during sintering. The thermal motion of molecules depends on temperature, and, according to Boltzmann's law of distribution, the number of molecules with higher energies increases as the temperature rises. These high-energy molecules have a greater likelihood of overcoming surface tension, which could lead to the release of vapor molecules and an elevation in vapor pressure. According to Kuczynski's two-sphere model^[31], the neck growth rate is defined as follows:

$$\frac{x}{r} = \left(\frac{3\sqrt{\pi} r M^{\frac{2}{3}} P_0}{\sqrt{2} R^{\frac{2}{3}} T^{\frac{2}{3}} d^2} \right)^{\frac{1}{3}} \cdot r^{\frac{2}{3}} t^{\frac{1}{3}} \quad (5)$$

where $\frac{x}{r}$ is the neck growth rate of the contact area of the spherical particles, x is the neck radius, r is the particle radius, M is the relative molecular weight, P_0 is the vapor pressure at the surface of the spherical particles, R is the gas constant, d is the particle diameter, T is the temperature, and t is the time. According to the equation, increasing the sintering temperature (T) from

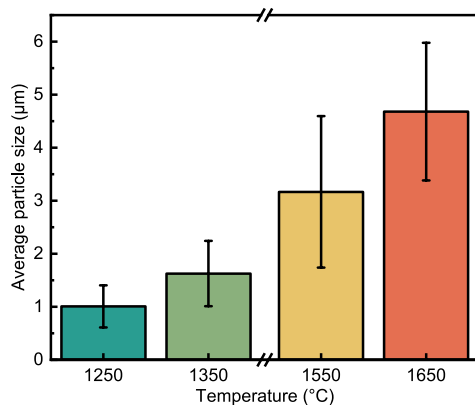


Fig. 8: Average particle size of ceramic samples sintered at different temperatures

1,150 °C to 1,650 °C accelerates the neck growth rate of spherical particles. This acceleration facilitates intergranular bonding, leading to a significantly larger average particle size within the sample. This aligns with the results obtained from the SEM images, i.e., different sintering temperatures have a significant impact on the microstructure of the ceramic samples.

The surface topography of ceramics significantly impacts their properties and applications. It can provide details on flatness, curvature, convexity, and unevenness of the surface^[32]. Figures 9 and 10 depict the 2D and 3D surface topography of the ceramic samples at varying sintering temperatures, respectively. As shown in Fig. 9, the ceramic samples exhibit delamination after sintering at all temperatures. At a sintering temperature of 1,350 °C, the samples exhibit significant cracks and protrusions on both sides of the cracks. This finding is in line with the results depicted in the SEM images in Fig. 5. As illustrated in Fig. 10, the surface morphology of the ceramic samples is smoother at higher sintering temperatures. This is due to the fact that at higher temperatures, the diffusion rate of molecules or atoms increases. Defects on the surface of the material, such as holes, pits, and clusters, are filled or diffused to other locations more quickly. An increase in temperature decreases the surface energy. This causes the structures on the surface of ceramic to rearrange due to the thermal movement of molecules or atoms, further reducing the surface energy and helping to lower the surface tension. As a result, the surface becomes smoother with fewer irregular particles. At the sintering temperature of 1,350 °C, the samples exhibit greater surface unevenness due to cracks, leading to poor surface quality.

Surface roughness reflects the degree of minor undulations and irregularities in the surface topography, and is a crucial aspect of surface topography information^[33]. Figure 11 illustrates the changes in surface roughness of the samples along the X and Y directions after sintering at different temperatures. An increase in sintering temperature leads to a decrease in surface roughness in both directions. According to Fig. 6, it is evident that the spacing between the layers of the samples gradually decrease with increasing sintering temperature, and this spacing has a significant impact on the surface roughness of the samples. Reducing the spacing between layers leads to diminished visible interfaces or step effects among printed layers, resulting in a smoother transition from layer to layer and a marked improvement in surface quality and smoothness. Figure 7 reveals that as the temperature increases, the bonding between the ceramic particles is strengthened, leading to the formation of larger crystalline particles. This process of particle aggregation fills surface gaps and pores, leading to a flattened and more even surface and a decrease in surface roughness of the ceramic sample. It is worth noting that the presence of large cracks in the samples at a sintering temperature of 1,350 °C leads to an increase in surface roughness. In general, an increase in sintering temperature usually results in a decrease in the surface roughness of ceramic samples. Therefore, adjusting the sintering temperature can enhance the flatness and quality of the ceramic surface.

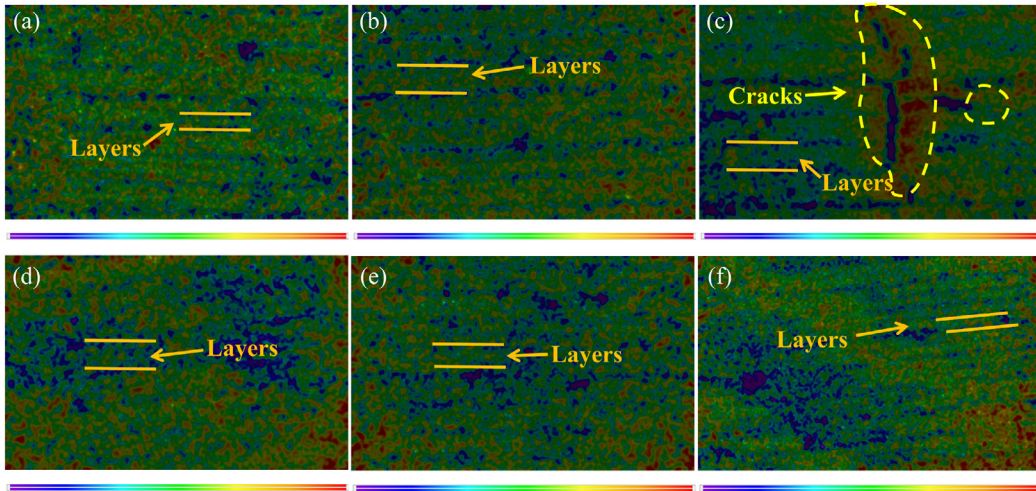


Fig. 9: 2D surface topography of ceramic samples after sintering at 1,150 °C (a); 1,250 °C (b); 1,350 °C (c); 1,450 °C (d); 1,550 °C (e); and 1,650 °C (f)

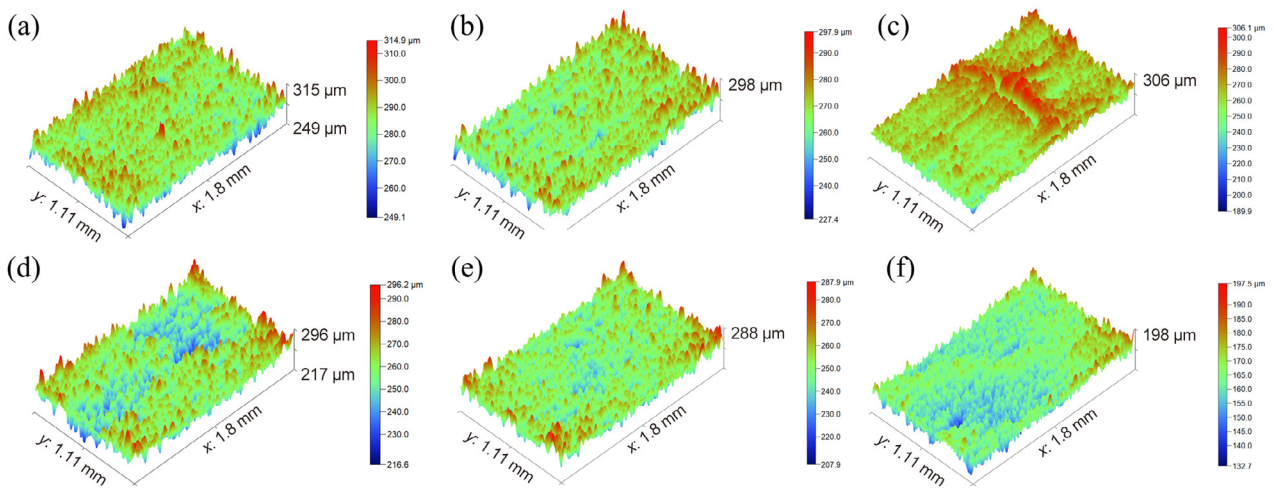


Fig. 10: 3D surface topography of ceramic samples after sintering at 1,150 °C (a); 1,250 °C (b); 1,350 °C (c); 1,450 °C (d); 1,550 °C (e); and 1,650 °C (f)

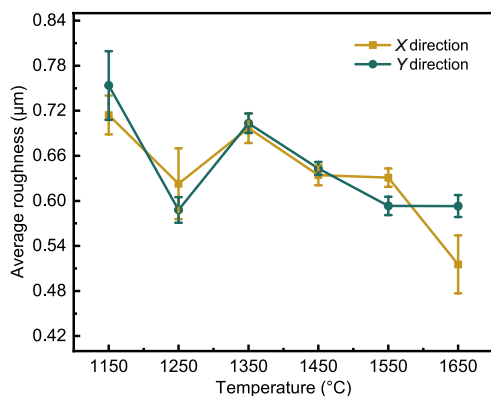


Fig. 11: Surface roughness of samples in the X and Y directions after sintering at different temperatures

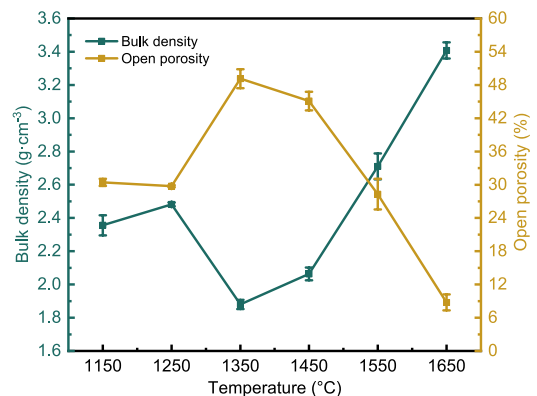


Fig. 12: Bulk density and open porosity of alumina ceramic samples sintered at different temperatures

3.3 Physical properties

Figure 12 displays the curves for bulk density and open porosity of alumina ceramic samples sintered at different temperatures. The ceramic samples show a decrease in open porosity and an increase in bulk density as the sintering

temperature rises from 1,150 °C to 1,250 °C. This is because the rate of diffusion among ceramic particles increases as the temperature rises, making atoms or molecules more likely to bridge the inter-particle gaps and rearrange into tighter positions. This interparticle diffusion facilitates the filling of voids and

pores between particles, thereby increasing the density of the ceramic sample^[34, 35]. However, the SEM image in Fig. 7 reveals that the ceramic samples transform from spherical to a plate-like structure. Additionally, the number of pores increases when the sintering temperature rises from 1,250 °C to 1,350 °C, leading to a higher porosity of the ceramics. As the sintering temperature increases from 1,350 °C to 1,650 °C, the samples become more compact, showing a gradual decrease in porosity and a gradual increase in bulk density. It is evident that the trend of open porosity shows a negative correlation with bulk density. Higher open porosity results in a greater number of pores in the sample, which leads to a lower bulk density. The balance between porosity and density can be achieved by controlling the sintering temperature.

3.4 Mechanical properties

Figure 13 displays the flexural strength of alumina ceramic specimens in the *X* and *Y* directions at different sintering temperatures. The relationship between flexural strength and sintering temperature follows a similar pattern to the relationship between bulk density and sintering temperature. At a sintering temperature of 1,150 °C, the flexural strength is at its lowest value in both the *X* and *Y* directions, measuring 17.91 MPa and 19.13 MPa, respectively. At the same time, a flexural strength of the ceramics greater than 20 MPa is achieved at the other sintering temperatures. According to the equation for the sintered diffusion coefficient^[36, 37]:

$$D = \frac{v\lambda^2}{6} \exp\left(\frac{-q}{kT}\right) \quad (6)$$

where *q* represents the activation energy for atomic diffusion, *v* denotes the frequency of atomic jumps, and λ is the distance of atomic jumps. When the sintering temperature *T* is increased from 1,150 °C to 1,650 °C, an increase of the diffusion coefficient *D* of the atoms is observed. Greater energy can be provided at a temperature of 1,650 °C, which facilitates the diffusion and bonding processes of the raw ceramic particles. The increased thermal movement of atoms and particles at elevated temperatures promotes interatomic diffusion, thereby driving the sinter-densification process, leading to enhanced flexural strength. It is worth noting that the lower flexural strength at a sintering temperature of 1,350 °C is not only due

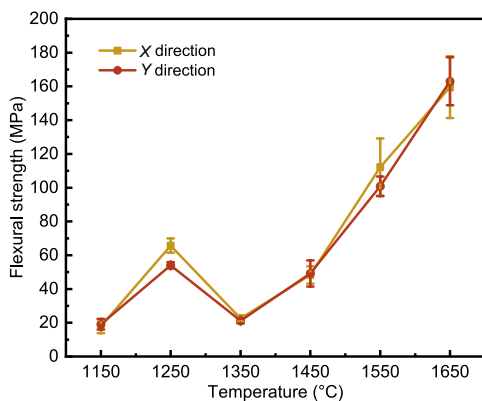


Fig. 13: Flexural strength of alumina ceramic samples at different sintering temperatures

to the alteration in grain shape but could also be attributed to the presence of larger cracks on the sample surface. Based on the results of the previous analyses (Fig. 8), it can be seen that the average grain size of the samples increases with the increasing sintering temperature. As the sintering temperature increases, the spacing between layers in the samples decreases (Fig. 6). This reduction in interlayer distance decreases the shear and interfacial stresses between the layers, ultimately enhancing the strength of the samples. Lower porosity or higher bulk density typically correlates with greater flexural strength. Porosity can lead to stress concentrations that weaken the ceramics, whereas higher density ceramic structures can improve inter-particle bond strength. There also seems to be a correlation between higher sintering temperatures and lower surface roughness (Fig. 11). The smoother surface can reduce stress concentrations and crack initiation points, thereby enhancing the flexural strength of ceramics.

Figure 14 displays the force-displacement diagrams from the bending tests of the samples sintered at 1,250 °C; 1,350 °C; 1,550 °C; and 1,650 °C. A force-displacement curve illustrates the influence of the applied stress on objects^[38]. It is evident from the curves that displacement increases proportionally with the load. The stiffness of the samples is minimized at a sintering temperature of 1,350 °C. This phenomenon happens because the presence of cracking defects within the ceramic that reduces its overall stiffness. This leads to stress concentrations, making the material more susceptible to deformation or cracks. In addition, the stiffness of the ceramic increases as the sintering temperature rises. When the sintering temperature is low, the internal grains of the sample are not tightly connected, and the sample may have large gaps or elastic volume, resulting in a lower overall stiffness. Increasing the sintering temperature results in larger grain size and decreased porosity, which in turn increases the stiffness of the samples. The insert in Fig. 14 displays a partial enlargement of the red boxed segment of the curve, which is partially serrated, at a sintering temperature of 1,650 °C. Delamination of the sample can lead to suboptimal bonding between different

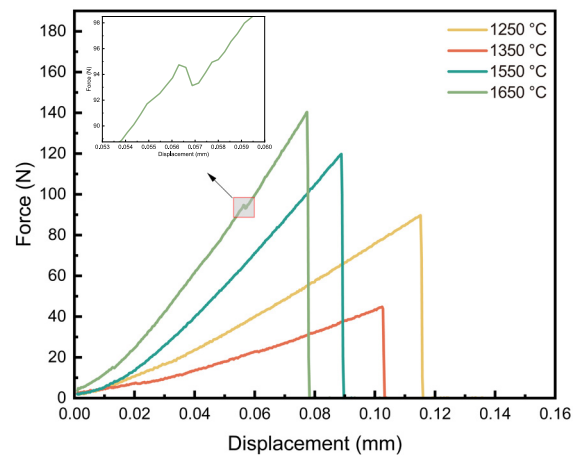


Fig. 14: Force-displacement curves for bending tests of samples sintered at 1,250 °C; 1,350 °C; 1,550 °C; and 1,650 °C. The inset is the enlarged region indicated by the red rectangle

layers, resulting in weaker interlayer bonding. When bending loads are applied, weaker interlaminar bonding can lead to sliding or relative displacement between the layers, ultimately increasing the overall displacement. Due to weakened interlayer bonding, the load is not adequately transferred to the next layer, resulting in a lower load value.

3.5 Friction and wear properties

Figure 15 illustrates the variations in the friction coefficient of the samples during a 10 min period of friction wear at different sintering temperatures. The friction curve fluctuates significantly during the initial stage of the test before gradually stabilizing in the later stages. The magnitude of this fluctuation indicates the smoothness of the friction process. In addition, the coefficient of friction for the samples increases and stabilizes during the wear process before reaching the sintering temperature of 1,350 °C, and decreases and stabilizes after

surpassing the sintering temperature of 1,350 °C. This is related to the contact conditions at the material's surface. When using small grinding balls, the contact area is reduced. As a result, there is a significant tangential resistance between the friction surfaces, which can lead to rapid wear and fluctuations in the coefficient of friction under a load [39]. During the friction process, the peaks of the wear surface roughness gradually smooth out and the contact area between the frictional components tends towards a fixed value. Simultaneously, the contact state of the material's surface gradually adapts to the working environment and stabilizes, leading to the material exhibiting consistent friction and wear performance. The friction coefficient values for all samples at all sintering temperatures range from 0.3 to 0.6. In addition, the friction and wear process of the samples becomes smoother when the sintering temperature exceeds 1,450 °C.

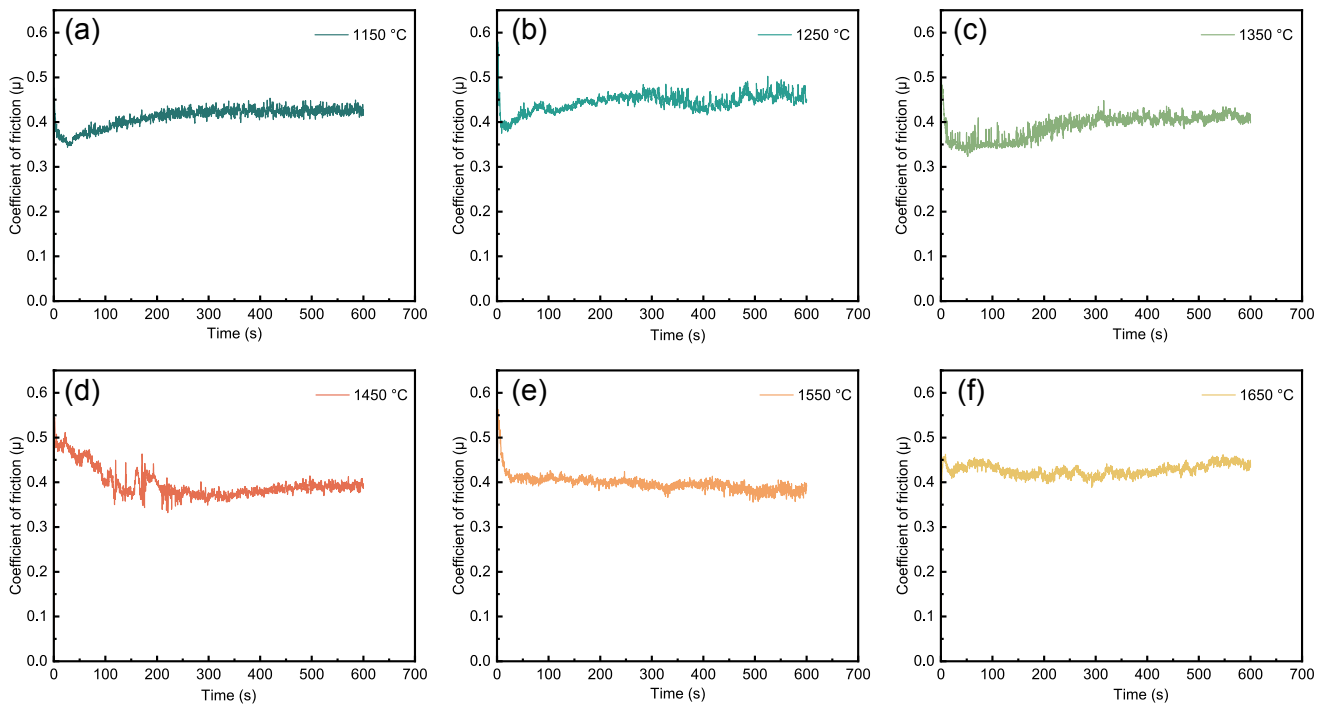


Fig. 15: Coefficient of friction (COF) during friction wear for samples sintered at 1,150 °C (a); 1,250 °C (b); 1,350 °C (c); 1,450 °C (d); 1,550 °C (e); 1,650 °C (f)

Figure 16 displays the variation curves of the average friction coefficient of the samples at various sintering temperatures. In general, the average friction coefficient of the samples increases with increasing sintering temperatures [40]. However, the friction coefficient of the samples decreases as the sintering temperature increases from 1,250 °C to 1,350 °C. This change is attributed to the transformation of the grain morphology in ceramics from spherical to plate-like, resulting in an increased contact area between the grains. Plate-like grains offer more contact points and surfaces, leading to an increase in the effective contact area during friction. The friction can be dispersed over a larger contact area under the same external loading conditions. This reduces the frictional stress per unit contact area and, consequently, the coefficient of friction.

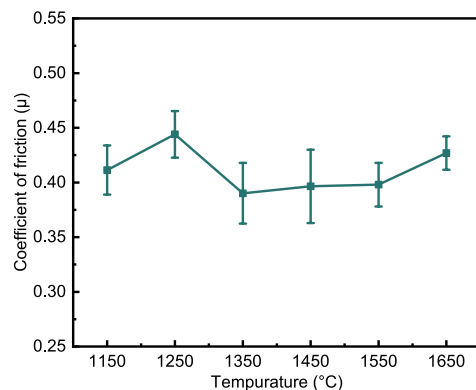


Fig. 16: Variation of the average coefficient of friction of samples sintered at different temperatures

Although the bulk density of ceramics decreases when cracks appear after sintering at 1,350 °C, cracks can disperse stresses from the crack tip to the surrounding area during friction, helping to alleviate the concentration of contact pressure between friction surfaces. This reduces the local stresses in the friction process and further reduces the coefficient of friction. With an increase in temperature, the bulk density of ceramics increases, leading to higher hardness and strength of ceramic materials, while reducing their local deformation ability. This implies that during friction, the ceramic material finds it more challenging to deform and adjust to the microscopic unevenness between surfaces. This, in turn, leads to an increase in friction and the coefficient of friction. Cheng et al. [41] embedded PMMA/PAO6 microcapsules into porous alumina ceramics to improve lubrication. The incorporation of microcapsules led to a significant decrease in the lowest coefficient of friction of porous alumina ceramics from 0.962 to 0.196. Li et al. [42] strengthened alumina ceramics by incorporating copper-doped zirconium oxide. Significant improvements were observed in the toughness and tribological properties of Cu/ZTA ceramics containing 5.0wt.% Cu, with the coefficient of friction decreasing from 0.43 to 0.38. Zhu et al. [43] utilized the SLA technique to fabricate zirconia-toughened alumina ceramics for dental purposes, and subsequently sintered them at varying temperatures of 1,450 °C; 1,550 °C; and 1,650 °C. The findings demonstrated a correlation between increased temperature and improved frictional characteristics. All samples exhibited coefficients of friction ranging from 0.2 to 0.4 at all temperatures when exposed to an artificial saliva environment. Based on the above reports, it has been found that researchers have employed various methods to reduce the friction coefficient of ceramics for broader applications. In this study, the material exhibited superior friction properties under high-temperature conditions, which is consistent with the previous report.

Figures 17 and 18 depict the 2D and 3D surface topography

of ceramic samples sintered at various temperatures after undergoing frictional wear. When the temperature reaches 1,150 °C, the surface of the sample shows obvious abrasion in the form of deeper pits, indicating poor resistance to abrasion. This is due to micro-convex fracture and grain pull-out during repeated contact friction experienced by the micro-convex body. As the temperature increases, the surface of the worn zones becomes less smooth. The roughness of the worn surfaces increases, and the worn morphology changes from deep pits to shallow grooves. Increasing the sintering temperature reduces the wear loss of the samples. When the temperature reaches 1,550 °C, the wear depth and wear width decrease further, and the worn morphology changes from a deep pit to a groove. This is largely because the temperature is directly proportional to the strength and density of the samples, a high sintering temperature results in a more uniform and compact ceramic structure, increased grain size, and stabilized friction. Higher densities have the potential to significantly enhance mechanical properties while minimizing defects in the ceramic microstructure. The small particles in the material are weakly bonded to the matrix, potentially causing damage by remaining at the interface after exfoliation. While, the large particles are firmly bonded to the matrix with high hardness, leading to a significant improvement in the wear resistance of the material. This finding aligns with the research by Cho et al. [44]. Higher sintering temperatures are preferred for alumina ceramics when they are used in conditions involving wear.

4 Conclusions

The sintering temperature is a crucial factor in ensuring the optimal performance of ceramic printed parts. This study examines the impact of sintering temperature on the microstructure and various properties of SLA 3D printed alumina ceramics. The microstructure of alumina changes as

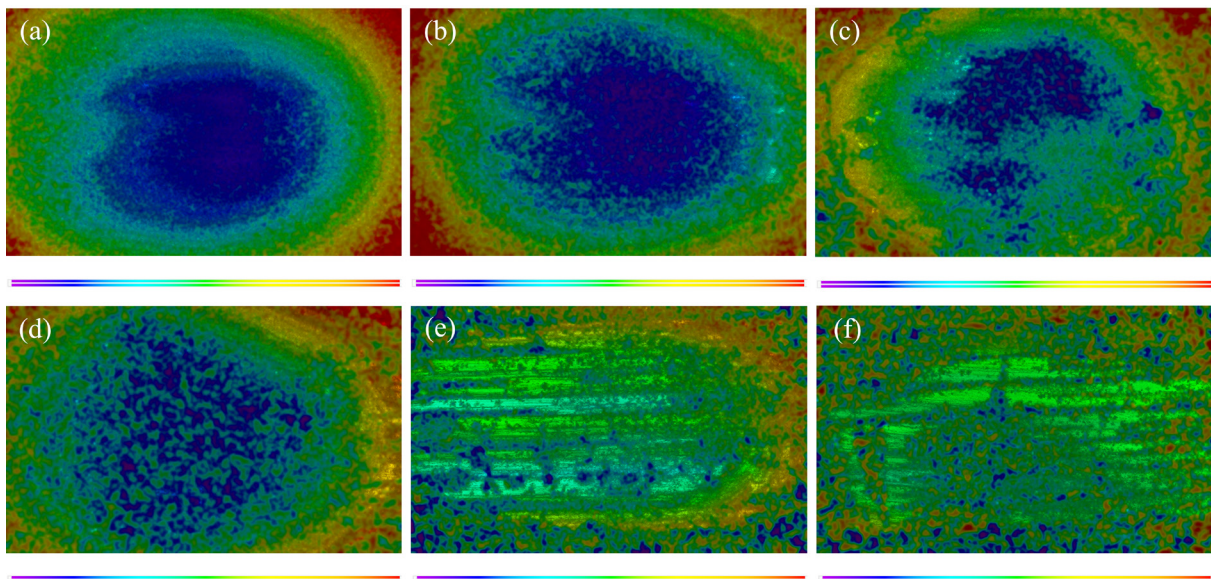


Fig. 17: 2D surface topography after friction wear of samples sintered at 1,150 °C (a); 1,250 °C (b); 1,350 °C (c); 1,450 °C (d); 1,550 °C (e); 1,650 °C (f)

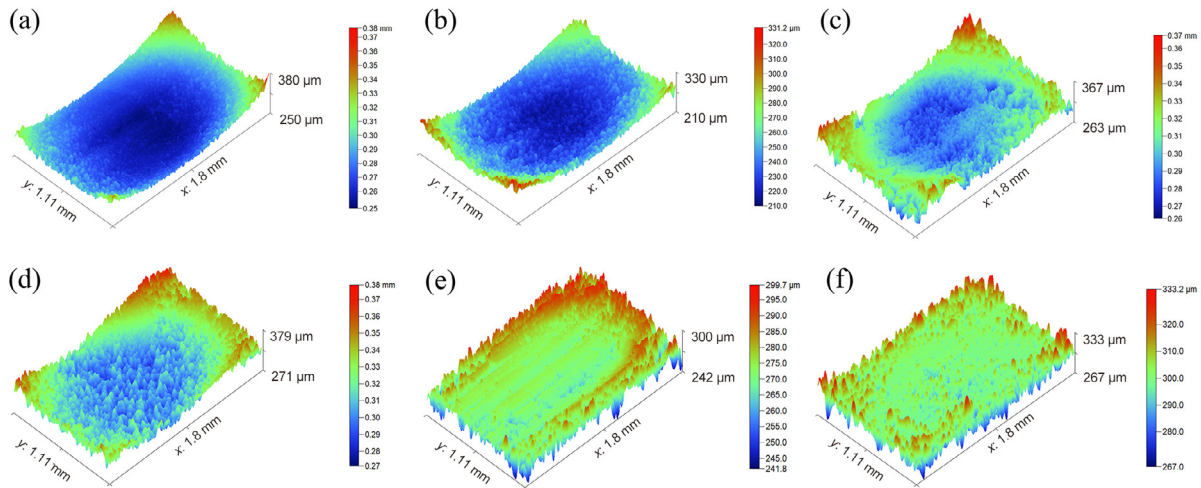


Fig. 18: 3D surface topography after friction wear of samples sintered at 1,150 °C (a); 1,250 °C (b); 1,350 °C (c); 1,450 °C (d); 1,550 °C (e); 1,650 °C (f)

the sintering temperature increases. At a sintering temperature of 1,350 °C, the morphology of the grains within the ceramics transitions from spherical to plate-like, resulting in large cracks. In addition to changes in the microstructure, the samples increase in density, and the surface roughness decreases as the sintering temperature increases. The increase in sintering temperature decreases the porosity of the samples. The ceramics sintered at temperatures below 1,650 °C have an open porosity of above 20vol.%, which decrease to below 10vol.% at the highest sintering temperature of 1,650 °C. The sample's flexural strength reaches the lowest and highest values at 1,150 °C and 1,650 °C, respectively. In addition, with an increasing sintering temperature, the abrasion marks on the samples during frictional abrasion transform from deep pits to shallow grooves. This results in a gradual decrease in the amount of abrasion and thus an increase in the material's abrasion resistance. Therefore, by optimizing the sintering temperature, ceramics that meet the requirements for various properties based on a target application can be obtained. This study lays the experimental groundwork for enhancing the properties of 3D printed alumina ceramics, which are benefit for engineering applications.

Acknowledgments

This work was supported by the Xinjiang Tianchi Talent Introduction Plan (51052300585), the Fundamental Research Funds for Autonomous Region Universities (XJEDU2022P002), the Natural science foundation project of Xinjiang Uygur Autonomous Region (2023D01C192, 2023D01C33), and the Tianshan Innovation Team Program of Xinjiang Uygur Autonomous Region (2023D14001).

Conflict of interest

The authors declare that they have no known competing financial interests or personal relationships that could have influenced the work reported in this paper.

References

- [1] Chen S, Sun D, Wang C S, et al. Alumina-based ceramic mold with integral core and shell for hollow turbine blades fabricated by laser powder bed fusion. *Additive Manufacturing*, 2022, 58: 103046.
- [2] Ikesue A, Aung Y L. Anisotropic alumina ceramics with isotropic optical properties. *Journal of Advanced Ceramics*, 2023, 12(1): 72–81.
- [3] Dong W J, Li Q L, Chen T C, et al. Effect of sintering temperature on microstructure and properties of 3D printing polysilazane reinforced Al₂O₃ core. *China Foundry*, 2023, 20(5): 387–394.
- [4] Liu X F, Guo X L, Shui G Y, et al. Properties of alumina-based ceramic cores. *China Foundry*, 2021, 18(6): 593–598.
- [5] Doi K, Mibe T, Matsui H. Brake judder reduction technology-brake design technique including friction material formulation. *JSAE Review*, 2000, 21(4): 497–502.
- [6] Matějka V, Lu Y F, Jiao L, et al. Effects of silicon carbide particle sizes on friction-wear properties of friction composites designed for car brake lining applications. *Tribology International*, 2010, 43: 144–151.
- [7] Zhang X Q, Zhang K Q, Zhang B, et al. Mechanical properties of additively-manufactured cellular ceramic structures: A comprehensive study. *Journal of Advanced Ceramics*, 2022, 11: 1918–1931.
- [8] Li H, Elsayed H, Colombo P. Enhanced mechanical properties of 3D printed alumina ceramics by using sintering aids. *Ceramics International*, 2023, 49: 24960–24971.
- [9] Song C K, Chen L F, Liu Y S. Long-term ceramic matrix composite for aeroengine. *Journal of Advanced Ceramics*, 2022, 11(9): 1343–1374.
- [10] Pan Z P, Guo J Z, Li S M, et al. Effect of nonuniform sintering on mechanical and thermal properties of silica-based ceramic cores. *China Foundry*, 2021, 18(5): 457–462.
- [11] Wu B, Liang J J, Yang Y H, et al. Phase constitution, microstructure and mechanical properties of a Ni-based superalloy specially designed for additive manufacturing. *China Foundry*, 2021, 18(4): 397–408.
- [12] Li H, Liu Y S, Liu Y S, et al. Influence of debinding holding time on mechanical properties of 3D-printed alumina ceramic cores. *Ceramics International*, 2021, 47: 4884–4894.
- [13] Zhou M P, Liu W, Wu H D, et al. Preparation of a defect-free alumina cutting tool via additive manufacturing based on stereolithography-optimization of the the drying and debinding processes. *Ceramics International*, 2016, 42(10): 11598–11602.

- [14] Cao J C, Li K, Luan T, et al. The Effect of high temperature heat treatment on fused silica ceramics. *Advanced Ceramics*, 2023, 44: 210–217.
- [15] Li H, Liu Y S, Liu Y S, et al. Influence of sintering temperature and CVI time on mechanical properties of 3D printed alumina ceramics. *Materials Letters*, 2021, 285: 129096.
- [16] Yang Z G, Yin Z Q, Wang D H, et al. Effects of ternary sintering aids and sintering parameters on properties of alumina ceramics based on orthogonal test method. *Materials Chemistry and Physics*, 2020, 241: 122453–122465.
- [17] Zhu C X, Cao F, Xiang Y, et al. Effects of sintering temperature on mechanical properties of alumina fiber reinforced alumina matrix composites. *Journal of Sol-gel Science and Technology*, 2019, 93(1): 185–192.
- [18] Li H, Liu Y S, Liu Y S, et al. Influence of vacuum debinding temperature on microstructure and mechanical properties of three-dimensional-printed alumina via stereolithography. *3D Printing and Additive Manufacturing*, 2020, 7(1): 8–18.
- [19] Li H, Liu Y S, Liu Y S, et al. Influence of sintering temperature on microstructure and mechanical properties of Al_2O_3 ceramic via 3D stereolithography. *Acta Metallurgica Sinica – English Letters*, 2020, 33(2): 204–214.
- [20] Hatanaka L C, Wang Q S, Cheng Z D, et al. Effect of trimethylolpropane triacrylate cross-linkages on the thermal stability and char yield of poly (methyl methacrylate) nanocomposites. *Fire Safety Journal*, 2017, 87: 65–70.
- [21] Gu Y, Duan W Y, Wang T C, et al. Additive manufacturing of Al_2O_3 ceramic core with applicable microstructure and mechanical properties via digital light processing of high solid loading slurry. *Ceramics International*, 2023, 49(15): 25216–25224.
- [22] Sotov A, Kantyukov A, Popovich A, et al. LCD-SLA 3D printing of BaTiO_3 piezoelectric ceramics. *Ceramics International*, 2021, 47(21): 30358–30366.
- [23] Dong D, Su H J, Li X, et al. Microstructures and mechanical properties of biphasic calcium phosphate bioceramics fabricated by SLA 3D printing. *Journal of Manufacturing Processes*, 2022, 81: 433–443.
- [24] Yu T L, Zhao Z, Li J C. Effect of sintering temperature and sintering additives on the properties of alumina ceramics fabricated by binder jetting. *Ceramics International*, 2023, 49(6): 9948–9955.
- [25] Xing Z W, Liu W W, Chen Y, et al. Effect of plasticizer on the fabrication and properties of alumina ceramic by stereolithography-based additive manufacturing. *Ceramics International*, 2018, 44(16): 19939–19944.
- [26] Zhang L, Huang J Y, Xiao Z H, et al. Effects of debinding condition on microstructure and densification of alumina ceramics shaped with photopolymerization-based additive manufacturing technology. *Ceramics International*, 2022, 48(10): 14026–14038.
- [27] Chen Z W, Liu C B, Li J J, et al. Mechanical properties and microstructures of 3D printed bulk cordierite parts. *Ceramics International*, 2019, 45(15): 19257–19267.
- [28] Su R Y, Chen J Y, Zhang X Q, et al. Accuracy controlling and mechanical behaviors of precursor-derived ceramic SiOC microlattices by projection micro stereolithography (μPSL) 3D printing. *Journal of Advanced Ceramics*, 2023, 12(11): 2134–2147.
- [29] Bae C J, Ramachandran A, Chung K, et al. Ceramic stereolithography: Additive manufacturing for 3D complex ceramic structures. *Journal of Korean Ceramic Society*, 2017, 54(6): 470–477.
- [30] Li J G, Ye Y P. Densification and grain growth of Al_2O_3 nanoceramics during pressureless sintering. *Journal of American Ceramic Society*, 2006, 89(1): 139–143.
- [31] Kuczynski G C. Self-diffusion in sintering of metallic particles. *Sintering Key Papers*, 1990: 509–527.
- [32] Pu Y Z, Zhao Y G, Zhang H Y, et al. Study on the three-dimensional topography of the machined surface in laser-assisted machining of Si_3N_4 ceramics under different material removal modes. *Ceramics International*, 2020, 46(5): 5695–5705.
- [33] Sedlaček M, Podgornik B, Vižintin J. Influence of surface preparation on roughness parameters, friction and wear. *Wear*, 2009, 266(3): 482–487.
- [34] Li H, Elsayed H, Colombo P. Effect of particle size distribution and printing parameters on alumina ceramics prepared by additive manufacturing. *Ceramics International*, 2024, 50(4): 6340–6348.
- [35] Huo M D, Li Q L, Liu J Q, et al. In-situ synthesis of high-performance Al_2O_3 -based ceramic cores reinforced with core-shell structures. *Ceramics International*, 2022, 48(22): 33693–33703.
- [36] Bordia R K, Kang S J L, Olevsky E A. Mechanical properties of additively-manufactured cellular ceramic structures: A comprehensive study. *Journal of Advanced Ceramics*, 2022, 11(12): 1918–1931.
- [37] Zhang Q Y, Chen M W, Qiu H P, et al. Effect of hot molding pressure on mechanical properties and behavior of SiC/SiC composites. *Advanced Ceramics*, 2023, 44: 50–56.
- [38] Wu Z C, Li S J, Fan X J, et al. In-situ preparation of robust self-lubricating composite coating from thermally sprayed ceramic template. *Journal of Advanced Ceramics*, 2023, 12(2): 357–372.
- [39] Li J C, Zhou Y C, Su Y F, et al. Synthesis and mechanical and elevated temperature tribological properties of a novel high-entropy (TiV Nb Mo W)C_(4.375) with carbon stoichiometry deviation. *Journal of Advanced Ceramics*, 2023, 12(2): 242–257.
- [40] Hisakado T, Tani H. Effects of elevated temperatures and topographies of worn surfaces on friction and wear of ceramics in vacuum. *Wear*, 1999, 224(1): 165–172.
- [41] Cheng Z Q, Gong H J, Wang Z, et al. Preparation of self-lubricating porous alumina ceramics with PMMA /PAO6 microcapsules and their tribological properties. *Ceramics International*, 2022, 48(6): 8031–8038.
- [42] Li Y X, Jing P P, Guo J, et al. Mechanical properties and wear behaviors of Cu-doped zirconia-toughened alumina ceramics. *Ceramics International*, 2023, 49(9): 14346–14354.
- [43] Zhu L, Xu Y D, Liu S W, et al. Microstructure, mechanical properties, friction and wear performance, and cytotoxicity of additively manufactured zirconia-toughened alumina for dental applications. *Composites, Part B: Engineering*, 2023, 250: 110459.
- [44] Cho K H, Jang H, Hong Y S, et al. The size effect of zircon particles zircon particles on the friction characteristics of brake lining materials. *Wear*, 2008, 264: 291–297.